JACS
JOURNAL OF THE AMERICAN CHEMICAL SOCIETY

Article

pubs.acs.org/JACS

Iron Pyrite Thin Films Synthesized from an $Fe(acac)_3$ Ink

Sean Seefeld,[†] Moritz Limpinsel,[†] Yu Liu,[‡] Nima Farhi,[§] Amanda Weber,[†] Yanning Zhang,[‡] Nicholas Berry,[‡] Yon Joo Kwon,[†] Craig L. Perkins,[∥] John C. Hemminger,[†] Ruqian Wu,[‡] and Matt Law*[,†,§]

[†]Department of Chemistry, [‡]Department of Physics and Astronomy, and [§]Department of Chemical Engineering and Materials Science, University of California, Irvine, Irvine, California 92697, United States

[∥]National Renewable Energy Laboratory, Golden, Colorado 80401, United States

Supporting Information

ABSTRACT: Iron pyrite (cubic FeS_2) is a promising candidate absorber material for earth-abundant thin-film solar cells. Here, we report on phase-pure, large-grain, and uniform polycrystalline pyrite films that are fabricated by solution-phase deposition of an iron(III) acetylacetonate molecular ink followed by sequential annealing in air, H_2S, and sulfur gas at temperatures up to 550 °C. Phase and elemental compositions of the films are characterized by conventional and synchrotron X-ray diffraction, Raman spectroscopy, Auger electron spectroscopy, secondary ion mass spectrometry, and X-ray photoelectron spectroscopy (XPS). These solution-deposited films have more oxygen and alkalis, less carbon and hydrogen, and smaller optical band gaps (E_g = 0.87 ± 0.05 eV) than similar films made by chemical vapor deposition. XPS is used to assess the chemical composition of the film surface before and after exposure to air and immersion in water to remove surface contaminants. Optical measurements of films rich in marcasite (orthorhombic FeS_2) show that marcasite has a band gap at least as large as pyrite and that the two polymorphs share similar absorptivity spectra, in excellent agreement with density functional theory models. Regardless of the marcasite and elemental impurity contents, all films show p-type, weakly activated transport with curved Arrhenius plots, a room-temperature resistivity of ∼1 Ω cm, and a hole mobility that is too small to measure by Hall effect. This universal electrical behavior strongly suggests that a common defect or a hole-rich surface layer governs the electrical properties of most FeS_2 thin films.

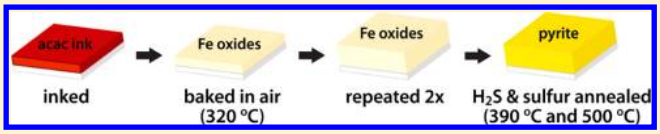

INTRODUCTION

Iron pyrite (cubic FeS_2) is experiencing renewed interest as an earth-abundant, nontoxic absorber layer for scalable thin-film photovoltaics (PV). Pyrite has an appropriate band gap (E_g ∼ 0.95 eV), very strong light absorption ($\alpha > 10^5$ cm^{-1} for $h\nu >$ 1.3−1.4 eV), and sufficiently long carrier drift and diffusion lengths to produce large short-circuit photocurrent densities (>30 mA cm^{-2}) in photoelectrochemical and solid-state Schottky solar cells based on pyrite single crystals.[1,2] The main limitation with pyrite is the low open-circuit voltage (V_{OC}) of pyrite devices, which does not exceed 200 mV or ∼20% of the band gap.[3] Efforts to correct this low V_{OC} require basic studies of high-quality bulk and thin-film pyrite samples.

Pyrite thin films have been fabricated by a variety of solution-phase and gas-phase methods (see refs 3 and 4 for summaries of the latter). Solution methods that leverage atmospheric-pressure, high-throughput, large-area processing techniques such as printing, roll coating, slit casting, or spraying may offer cost and scalability advantages relative to the vacuum-based batch processing traditionally employed in PV manufacturing.[5] Solution methods used to make pyrite thin films include spray pyrolysis,[6−10] electrodeposition,[11−16] chemical bath deposition (CBD),[17,18] electrophoretic deposition (EPD),[19] and sol gel chemistry.[20−22] The strategy adopted in most of these cases is to deposit a film of (often amorphous) iron oxides or iron sulfides and anneal the film in sulfur gas at elevated temperatures (350−600 °C) to produce polycrystalline pyrite. Table 1 compiles the principal reports of solution-deposited pyrite films, listing only those examples that provide substantive optical or electrical characterization of nominally phase-pure samples. Although many of these reports are partial and some present electrical data that is difficult to reconcile with results from other films and pyrite single crystals,[3,23] most conclude that unintentionally doped, solution-deposited pyrite films are p-type with low resistivity and low mobility, in agreement with results from samples grown by gas-phase methods.[4] Recently, pyrite films have also been made by the solution deposition of pyrite nanocrystals, either with or without postdeposition sintering to increase grain size and film density,[24−28] but the electrical properties of these films have not been reported in detail (see Table 1).

Molecular inks are an especially promising solution-phase approach for fabricating high-performance semiconductor thin films for PV.[5] A molecular ink is a concentrated solution of molecular precursors that is cast onto a substrate and annealed to form a film of a desired material. Pioneered by Mitzi for the synthesis of metal chalcogenides,[29] molecular inks may offer the following advantages: (i) simple and scalable processing; (ii) intermixing of precursors on a molecular level, resulting in

Received: December 12, 2012
Published: February 11, 2013

   dx.doi.org/10.1021/ja311974n | J. Am. Chem. Soc. 2013, 135, 4412−4424

Table 1. Synthesis and Properties of Solution-Deposited Pyrite Thin Films

method[a]	precursors	conditions	reported properties	ref
spray pyro	$FeCl_3$, thiourea (*aq.*)	550 °C in air (?), no anneal (?)	E_g = 1.05 eV	6
spray pyro	$FeCl_3$, thiourea (*aq.*)	350 °C in N_2 + S, no anneal	E_g = 0.82 eV, p-type,[b] low mobility, ρ = 0.16 Ω cm	7
spray pyro	$FeSO_4$, $(NH_4)_2S$ (*aq.*)	120 °C in air, 500 °C anneal in S	p-type,[c] p = 10^{16}–10^{20} cm^{-3}, μ = 1–200 cm^2 V^{-1} s^{-1} (?)	9
spray pyro	$FeCl_3$ (*aq.*)	350 °C in air, 450 °C anneal in S	E_g = 0.73 eV, ρ = 0.6 Ω cm, non-Arrhenius T dependence	10
spray pyro	$FeCl_3$ (*aq.*)	350 °C in air, 350 °C anneal in S	E_g = 0.93 eV, p-type[b]	8
electrodep	$Na_2S_2O_3$, $(NH_4)_2Fe(SO_4)_2$ (*aq.*)	60 °C, 500 °C anneal in S	n-type (due to Ti doping?)[b]	13
electrodep	$FeCl_2$, $Na_2S_2O_3$ (*aq.*)	25 °C, 500 °C anneal in S	E_g = 1.34 eV, p-type,[c] p = 10^{14} cm^{-3}, μ ∼ 200 cm^2 V^{-1} s^{-1} (?)	12
CBD	$Fe(CO)_5$, S in org solv	80–165 °C in argon, no anneal	photoactive	17
CBD	$FeSO_4$, en, $Na_2S_2O_3$ (*aq.*)	28 °C, 450 °C anneal in S	E_g = 0.94 eV, n-type (?)	18
EPD	$FeCl_3$, thiourea (*aq.*)	200 °C, no anneal	E_g = 1.19–1.40 eV, n-type (?)	19
sol gel	$Fe(NO_3)_3$ (*aq.*)	25 °C, 500 °C anneal in air +400 °C in S	E_g = 0.99 eV, p-type,[c] p = 10^{19} cm^{-3}, μ = 1.5 cm^2 V^{-1} s^{-1}	20
sol gel	$(NO_3)_3$, PO in EtOH (*aq.*)	25 °C, 100 °C anneal in air +450 °C in S	E_g = 0.93 eV	22
sol gel	$Fe(NO_3)_3$, acac in EG	40 °C, 500 °C anneal in air +400–600 °C in S	E_g = 0.77–0.87 eV, n-type w/low T anneal, p-type w/high T anneal[c]	21
NC	$FeCl_2$, TOPO, oleylamine	220 °C in argon, dip coating	E_g = 0.93 eV, p-type,[c] μ = 80 cm^2 V^{-1} s^{-1} (?)	25
molecular ink	$Fe(acac)_3$ + S in pyridine	25 °C, 320 °C in air, 390 °C in H_2S + 550 °C in S	E_g = 0.87 eV, p-type,[b] low mobility, ρ = 1.9 Ω cm	this work

[a]Spray pyro = spray pyrolysis; electrodep = electrodeposition; CBD = chemical bath deposition; EPD = electrophoretic deposition; NC = nanocrystal deposition; DEG = diethylene glycol; en = ethylenediamine; PO = propylene oxide; EG = ethylene glycol; acac = acetylacetone; TOPO = trioctylphosphine oxide; [b]By thermopower. [c]By Hall effect. (?) = incomplete or questionable data or conclusions.

uniform composition and excellent crystallinity in the finished film; (iii) good control of stoichiometry via ink composition; (iv) low concentrations of elemental impurities (e.g., oxygen, carbon, halides) for well-formulated, organic-free inks, such as those utilizing hydrazine (N_2H_4) as a solvent; (v) straightforward doping and alloying by spiking inks with desired elements; (vi) no need to synthesize, purify, assemble, and passivate nanocrystals. Hydrazine-based molecular inks have been used to fabricate $CuIn(Se,S)_2$ (CISSe), $CuIn_{1-x}Ga_xSe_2$ (CIGS), and Cu_2ZnSnS_4 (CZTS) solar cells with efficiencies as high as 12.2%, 12.8%, and 11.1%, respectively,[30−32] demonstrating the promise of this approach for PV applications.

Several molecular inks for pyrite are under development in our laboratory. Here, we report on the structural, optical, and electrical properties of pyrite thin films prepared from a molecular ink composed of $Fe(acac)_3$ (acac = acetylacetonate) and elemental sulfur in pyridine. This viscous, air-stable ink is spin coated onto a substrate, pyrolyzed to form a film of iron oxides and iron salts, then sulfurized to convert the oxides/salts to pyrite. Metal acetylacetonate inks have previously been used to make $CuInS_2$ films by roll coating.[33] Our $Fe(acac)_3$ ink avoids the use of toxic and explosive hydrazine at the cost of relatively high levels of oxygen (1750–8800 ppm) and some carbon (500–1000 ppm) in the final films. The sulfur-annealed films are pure-phase pyrite to within the detection limit of synchrotron X-ray diffraction (XRD) and Raman spectroscopy. Films grown on molybdenum-coated glass substrates consist of densely packed columnar grains and are uniform in thickness (±5%), fairly smooth (RMS roughness on the order of 10% of the film thickness), free of cracks and pinholes, and mechanically adherent and robust. Films grown on fused quartz substrates show optical band gaps of ∼0.87 eV and a maximum absorption coefficient of approximately 4 × 10^5 cm^{-1}. The electrical properties of these films (Table 1) are effectively identical to nearly all other unintentionally doped pyrite films. The universal electrical behavior of pyrite films is most likely caused by a conductive, hole-rich surface layer or trace amounts of nanoscale phase impurities undetectable by XRD and other bulk analytical techniques.

METHODS

Chemicals. Iron(III) acetylacetonate (≥99.9%) and anhydrous pyridine were purchased from Aldrich, sulfur (99.995%) from Alfa Aesar, and hydrogen sulfide (99.3%) from Airgas. Electronic grade acetone (Aldrich) and HPLC-grade isopropanol (Fisher) were used for cleaning substrates. All chemicals were used as received.

Film Fabrication. A spin-coating ink was prepared by dissolving 0.7 g of Fe(III) acetylacetonate (2 mmol) and 0.1 g of elemental sulfur (3.1 mmol) in 2 mL of pyridine and sonicating the mixture at 50 °C for 6 h. Molybdenum-coated glass substrates were used as received, while fused quartz substrates were cleaned by sonication in acetone and isopropanol. Ink films were made by spin coating 175 μL of the solution onto clean 1 $in.^2$ substrates (2000 rpm for 60 s) in a N_2-filled glovebox. The sample was then placed on a cold hot plate and heated in air to 320 °C (for 1 mm thick substrates) or 370 °C (for 3 mm thick substrates) over the course of 10 min, after which it was immediately moved to the edge of the hot plate to cool for 5–10 s and placed in a cool Petri dish. Two additional deposition and baking steps were used to produce films with a target pyrite thickness of ∼300 nm. The ink films were then annealed in 1 atm of flowing H_2S gas (390 °C for 12 h) to yield mixed-phase pyrite/marcasite thin films ("H_2S annealed" films). The marcasite impurity was eliminated by annealing the films in evacuated 125 × 14 mm^2 quartz ampules containing 100 mg of elemental sulfur and 100 mTorr of argon.

Molybdenum-coated glass substrates were supplied by Prof. Chinho Park, Yeungnam University. Molybdenum-coated silicon substrates were made by in-house RF sputtering (99.95% Mo target, 5 × 10^{-6} Torr base pressure, 10 mTorr argon deposition pressure) onto undoped float zone silicon wafers.

Characterization. Powder XRD data were collected with a Rigaku Ultima III diffractometer using Cu Kα radiation and a 1° incidence angle in parallel beam geometry. Quantitative phase concentrations were established by simulating powder patterns with the PDXL software package (Rigaku Corporation) using the Rietveld refinement procedure. High-resolution synchrotron XRD was carried out on beamline 11-BM of the Advanced Photon Source at Argonne National Laboratory. Scanning electron microscopy (SEM) imaging employed an FEI Quanta 3D FEG operating at 5 kV. Prior to SEM imaging, samples on quartz were coated with ∼1 nm of Au/Pd using a Polaron

SC 7620 sputtering system. A Renishaw inVia confocal Raman microscope with less than 5 mW of 532 nm laser excitation and a 50× objective lens was used for Raman experiments. Ultraviolet−visible (UV−vis) optical absorption measurements were performed with a PerkinElmer Lambda 950 spectrophotometer equipped with a 60 mm integrating sphere. Films of ∼125 nm thickness were used for optical measurements. Fourier transform infrared (FTIR) spectroscopy was performed using a Nicolet 6700 instrument in transmission mode using double-side polished silicon substrates. Temperature-dependent resistivity and Hall effect data were acquired on an Ecopia HMS 5000 system using the van der Pauw method with currents of 0.2−5.0 μA. Ohmic contacts were made by evaporating 250 nm of Ag through a shadow mask in a glovebox thermal evaporator with a base pressure of 5×10^{-6} Torr. Qualitative thermopower measurements were carried out in a glovebox using a hot plate to establish an 80 K temperature gradient across the samples and a Keithley 2636 SourceMeter to determine the majority carrier type.

X-ray photoelectron spectroscopy (XPS) measurements were performed with an ES-CALAB MKII surface analysis instrument (VG Scientific). The ultrahigh vacuum (UHV) multichamber system is equipped with a twin anode X-ray source (Mg/Al) and a 150 mm hemispherical electron energy analyzer. Spectra presented here were collected using Al Kα X-rays (1486.6 eV) in constant energy mode with a pass energy of 20 eV. The base pressure of the spectroscopy chamber was 5×10^{-10} Torr during acquisition. Binding energies were calibrated by setting the Au $4f_{7/2}$ peak of a Au foil attached to the surface of the sample to 84.0 eV. Deconvolution and spectral line fitting were carried out using Shirley backgrounds and Voigt lineshapes in the XPSPeak 4.1 software package. Samples were briefly exposed to air during loading into the XPS chamber.

Secondary ion mass spectrometry (SIMS) was performed by Evans Analytical Group on a Cameca dynamic SIMS instrument using 14.5 keV Cs ions for anions (S, O, H, C, Si) and 8 keV O_2 ions for cations (Na, K, Mg, Ca, Al, Mo). Estimated detection limits were 2×10^{15} atoms/cm^3 for Na, K, Al, and Mg, 5×10^{15} atoms/cm^3 for Ca, 2×10^{18} atoms/cm^3 for C, 1×10^{19} atoms/cm^3 for O, and 2×10^{17} atoms/cm^3 for H. Atomic concentrations are accurate to within a factor of 5. The depth scale was quantified by measuring the analysis craters with a stylus profilometer and confirmed by SEM imaging of the sectioned films.

Auger electron spectroscopy (AES) measurements were performed using a modified Physical Electronics Model 670 field emission scanning Auger microprobe that has been described previously.[34] For depth profiling experiments, a 5 kV, 20 nA primary electron beam was used in conjunction with a 3 kV Ar^+ ion beam. Samples were rotated at 1 rpm during sputtering and data acquisition. Direct spectra were numerically smoothed and differentiated using the Savitsky−Golay algorithm.[35] Elemental intensities were corrected by literature sensitivity factors for our instrument, and the atomic concentration results were normalized to 100%.

RESULTS AND DISCUSSION

Synthesis and Structural Characterization. The ink used to prepare pyrite thin films in this study is a mixture of 1.0 M $Fe(acac)_3$ and 1.6 M sulfur in pyridine. Sulfur was used to increase the viscosity of the $Fe(acac)_3$ solution to enable the deposition of uniform, relatively thick layers (100−125 nm) by spin coating (see the Methods section). The processing sequence (Figure 1a) consists of three cycles of ink deposition and air baking followed by sequential annealing in H_2S and then sulfur gas to yield ∼300 nm thick pyrite films. This film thickness was chosen because it is sufficient to absorb >95% of photons with $h\nu$ > 1.25 eV in one optical pass. We found that both H_2S and sulfur annealing are required to make high-quality pyrite films: H_2S alone yields films of pyrite contaminated with marcasite (orthorhombic FeS_2), while direct sulfur annealing results in poor-quality, discontinuous pyrite

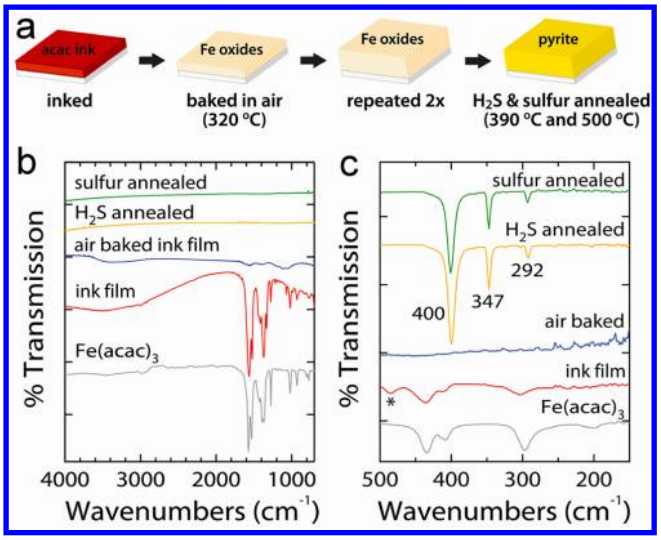

Figure 1. FTIR spectra of films at different stages of processing. (a) Film processing sequence. (b) Mid-IR spectra. (c) Far-IR spectra. Sample thickness: ∼125 nm. Films were prepared by single-layer spin coating onto double side polished silicon substrates. Air baking was carried out at 320 °C; H_2S annealing at 390 °C for 12 h; sulfur annealing at 500 °C for 4 h.

layers. Single-layer films were characterized by FTIR spectroscopy after each processing step in order to monitor the conversion of the $Fe(acac)_3$ ink films to iron oxides/salts and subsequent sulfurization of the iron oxides/salt films to pyrite (Figure 1b,c). Prior to heating, the orange-red dried ink layer has mid- and far-IR spectra essentially identical to that of an $Fe(acac)_3$ standard (red and gray plots in Figure 1b,c). The small peak at 485 cm^{-1} in the ink spectrum is assigned to sulfur (labeled with an asterisk, Figure 1c).[36] We conclude that the dried ink is mainly a simple mixture of $Fe(acac)_3$ and sulfur. Air baking to 320 °C results in a near flatlining of the mid- and far-IR spectra (blue curves). While a nonzero signal in the fingerprint region (900−1700 cm^{-1}) indicates the presence of organic residues in the film, it is clear that nearly all of the organics are decomposed and/or volatilized during air baking. Most of the sulfur evaporates too, and the rest is oxidized to sulfate (see below). As discussed in more detail below, XPS shows that the baked films are a mixture of iron oxides, sulfates, carbonates, and perhaps hydroxides (see orange spectra in Figure 6). These films are light brown in color and amorphous by XRD. Optical absorption spectra display clear $Fe(acac)_3$ absorption peaks before air baking; after air baking, the molecular features are lost, and the spectra show a monotonic absorption increase with an onset at ∼1.6 eV (see Figure S1 in the Supporting Information). Annealing the baked films in H_2S (1 atm, 390 °C for 12 h) converts the iron oxides/salts to pyrite (cubic FeS_2), as evidenced by the appearance of characteristic pyrite IR vibrations at 292, 347, and 400 cm^{-1}, contaminated with a small amount of marcasite. The mid-IR spectra of H_2S annealed films are completely featureless. Annealing these mixed-phase pyrite/marcasite films in sulfur vapor (∼0.65 atm, 500 °C for 4 h) converts marcasite to pyrite without causing additional changes to the IR spectra (green curves in Figure 1b,c).

FeS_2 films were prepared on fused quartz substrates and molybdenum-coated soda lime glass substrates and characterized by SEM, XRD, Raman spectroscopy, and XPS. Quartz is a useful substrate for optical and electrical studies, while Mo-

coated glass is a promising substrate for solar cell fabrication. Figure 2 shows SEM and XRD data for a 270 ± 30 nm thick

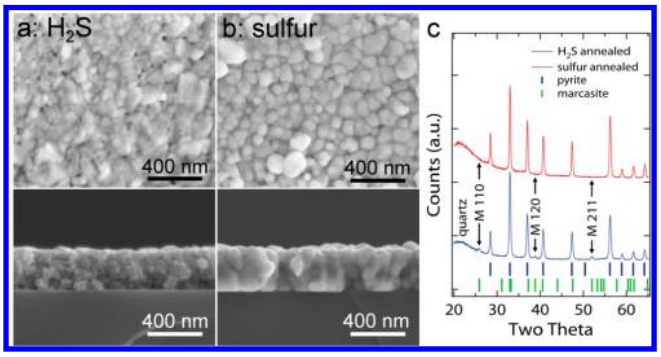

Figure 2. FeS_2 thin films on fused quartz substrates. Plan view and cross-sectional SEM images of a film (a) after H_2S annealing (390 °C for 12 h) and (b) after sulfur annealing (~0.65 atm of sulfur vapor at 500 °C for 4 h). (c) XRD patterns of the films, along with pyrite and marcasite reference powder patterns. The small marcasite impurity in the original film (indicated by the labels M 110, M 120, and M 211) is eliminated by sulfur annealing. See Figure S2 (Supporting Information) for higher-resolution XRD scans of a sulfur-annealed film on a quartz substrate.

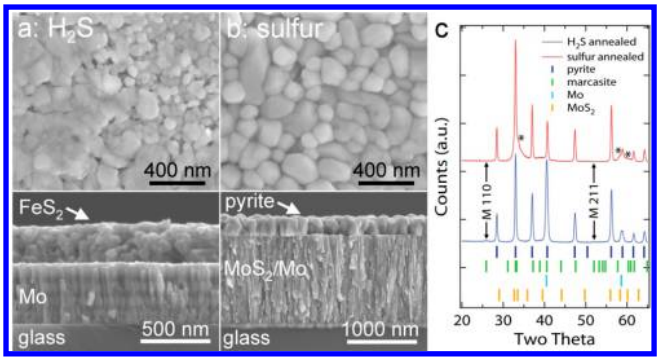

Figure 3. FeS_2 thin films on Mo-coated soda lime glass substrates. Plan view and cross-sectional SEM images of a film (a) after H_2S annealing (390 °C for 12 h) and (b) after sulfur annealing (~0.65 atm of sulfur vapor at 550 °C for 8 h). Sulfurization causes a substantial change in the morphology and composition of the underlying Mo layer. See Figures S3 and S4 (Supporting Information) for analysis of the Mo substrates. (c) XRD patterns of representative films before and after sulfur annealing, along with pyrite, marcasite, Mo, and MoS_2 reference powder patterns (MoS_2 PDF no. 00-037-1492). The slight marcasite impurity in the original film is eliminated by sulfur annealing. MoS_2 peaks are indicated by asterisks. See Figure S5 (Supporting Information) for higher-resolution XRD scans of a sulfur-annealed film on Mo-coated glass. Layer thicknesses: 270 nm for FeS_2 and pyrite layers, 440 nm for Mo before sulfur annealing, and 1280 nm for MoS_2/Mo after sulfur annealing.

film on quartz before and after sulfur annealing. Prior to sulfur annealing, these films consist of densely packed but small grains of pyrite mixed with a substantial fraction of marcasite (<10 vol %, as estimated by XRD pattern analysis; see the Methods section). XRD shows clear marcasite {110}, {120}, and {211} reflections. Sulfur annealing converts the marcasite to pyrite and results in significant grain growth, with apparent grain sizes of 50−150 nm as determined by SEM, in good agreement with the grain size determined by Scherrer analysis of synchrotron XRD patterns (100−150 nm). Pyrite is the only phase detected by XRD after sulfur annealing.

SEM and XRD data for a typical 270 ± 30 nm thick FeS_2 film on a Mo-coated glass substrate are shown in Figure 3. Prior to sulfur annealing, these films consist of densely packed, small grains of pyrite with a very small marcasite impurity evident in XRD. Sulfur annealing (in this case at 550 °C for 8 h) eliminates the marcasite and results in tightly packed columnar pyrite grains, with most grains extending across the entire film (apparent grain size: 270 nm tall × 100−250 nm wide), which is a favorable morphology for efficient charge collection in future pyrite solar cells. Sulfur annealing also converts some of the underlying Mo layer to MoS_2, leading in this particular film to a 3-fold volume expansion along the film normal necessary to accommodate the 3.4-fold larger 2H−MoS_2 unit cell (106.4 Å^3 for MoS_2 vs 31.2 Å^3 for Mo). The extent of Mo conversion can be controlled by tuning the sulfur annealing conditions, and we routinely obtain phase-pure pyrite films from the $Fe(acac)_3$ ink with only partial conversion of Mo to MoS_2 (i.e., MoS_2 on top, Mo underneath). Despite the dramatic volume expansion of the Mo layer, the pyrite films are mechanically robust and strongly adherent to the substrate, easily passing the common tape peel tests. Similar results were recently reported for pyrite films grown on Mo-coated glass by chemical vapor deposition (CVD).[4]

Figure 4 presents Raman spectra and high-resolution synchrotron XRD data to more rigorously assess the phase composition of the FeS_2 films. Raman spectroscopy is more sensitive than conventional XRD to marcasite impurities near

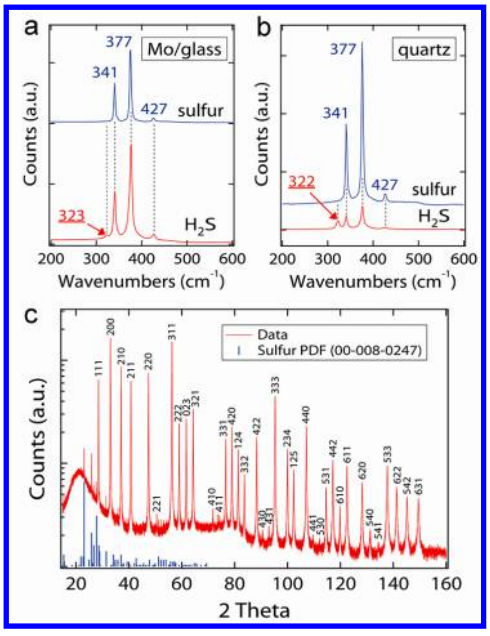

Figure 4. Phase composition by Raman spectroscopy and synchrotron XRD. Raman spectra of FeS_2 films on (a) Mo-coated glass and (b) quartz substrates before and after sulfur annealing ($\lambda_{incident}$ = 532 nm, giving a probe depth of ~45 nm). The label for the marcasite peak at ~323 cm^{-1} is underlined. H_2S-annealed films on quartz show a relatively large marcasite signal due to the absence of sodium in the substrate.[4] Annealing completely eliminates the marcasite impurity in both films. (c) Synchrotron XRD data on a log scale. All peaks index to pyrite (labeled with Miller indices) or orthorhombic sulfur (α-S, PDF no. 00-008-0247, blue lines). The broad feature at ~20° is due to the incorporation of amorphous quartz fragments into the sample during sample preparation. A least-squares fit of the first 20 peaks in the XRD pattern yields a pyrite lattice constant a = 5.41947 ± 0.00015 Å.

dx.doi.org/10.1021/ja311974n | J. Am. Chem. Soc. 2013, 135, 4412−4424

the film surface, while synchrotron-based capillary XRD is a uniquely sensitive technique for the detection of crystalline and amorphous phase impurities. H_2S-annealed films on Mo-coated glass and quartz substrates show Raman bands for both marcasite (at 323 cm^{-1}) and pyrite (at 341, 377, and 427 cm^{-1}, corresponding to the A_g, E_g, and $T_g(3)$ vibrational modes, respectively). Two additional pyrite T_g vibration bands are probably present but concealed by the large peaks at 341 and 377 cm^{-1}.[37−39] We note that films grown on quartz contain a larger fraction of marcasite relative to pyrite because of the very low concentration of sodium and other alkalis in the quartz substrates. Sodium leaching has been observed to promote pyrite nucleation and growth at the expense of marcasite, for unknown reasons.[4] Raman spectra of sulfur-annealed films show no sign of marcasite.

Synchrotron XRD was performed on beamline 11-BM of the Advanced Photon Source at Argonne National Laboratory in transmission mode on a sample made by loading a Kapton capillary with the powder scraped from eight sulfur-annealed films grown on quartz substrates. All peaks in the pattern index to either pyrite or α-sulfur, with no other phases detected (Figure 4c). This result shows that our $Fe(acac)_3$ ink approach consistently produces phase-pure pyrite films within the detection limits of state-of-the-art XRD. The trace sulfur contamination originates from occasional condensation of sulfur vapor onto the films as they cool after annealing.

AES and SIMS depth profiles were employed to determine the bulk elemental composition of sulfur-annealed pyrite films on Mo-coated glass and Mo-coated silicon substrates. Figure 5a,b shows AES and SIMS data for a 300 ± 30 nm thick pyrite film on Mo-coated glass. The AES depth profile indicates that the sample can be described a $FeS_2/MoO_{0.03}S_{1.97}/MoO_xS_{2-x}$/glass stack (with $x > 0.03$). A large amount of potassium and smaller amounts of sodium, oxygen, and carbon were detected at the surface of the film. Elevated levels of potassium and oxygen were observed at the pyrite/MoS_2 interface. All other elements were below AES detection limits (~0.1 atom %). The SIMS profiles in Figure 5b show the concentration of C, H, O, Na, K, Al, Ca, and Mg as a function of depth into the film stack. Raw ion counts for three matrix elements (S, Mo, and Si) are also plotted to track position within the film stack. Average impurity concentrations in the pyrite layer are listed in Table 2 and compared to a similar film made by CVD.[4] The largest impurity is oxygen (~0.9 atom %), followed by potassium (0.4%), sodium (0.14%), carbon (0.05%), hydrogen (0.034%), aluminum (0.016%), calcium (~10 ppm), and magnesium (<1 ppm), giving a total impurity load of approximately 1.5 atom %. Our measurements do not reveal much about the location of these elements in the film, that is, whether they are substitutional impurities, interstitials, defect clusters, amorphous nanoscale phase domains (e.g., amorphous Fe_2O_3) or segregated species at the surfaces and grain boundaries. In the unlikely case that the 0.9 atom % oxygen is uniformly distributed on sulfur sites (O_S impurities), we expect a stoichiometry of $FeO_{0.027}S_{1.973}$, which is in any case too light in oxygen to observe the increased band gap of iron oxysulfide alloys predicted by recent density functional theory (DFT) calculations (see below).[40] Note that, due to our experimental conditions and the lack of SIMS standards for pyrite, we estimate that the concentrations reported here are accurate only to within a factor of 5.

We find that oxygen levels are ~20 times higher while carbon and hydrogen levels are ~7 times lower for films made from

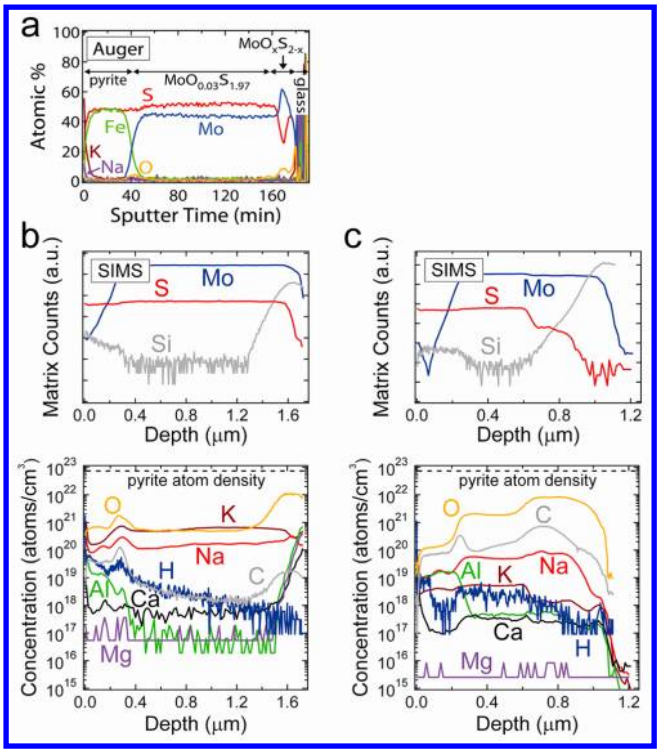

Figure 5. Bulk elemental composition of pyrite films. (a) AES depth profile of a 300 ± 30 nm thick pyrite film on Mo-coated glass. The sample can be described as a FeS_2/ $MoO_{0.03}S_{1.97}/MoO_xS_{2-x}$/glass stack. The AES profile shows the presence of K and Na at the pyrite surface and O and K at the FeS_2/MoS_2 interface. Carbon was detected only prior to sputtering and thus is not mapped. The relatively small sulfur signal is due to preferential sputtering of sulfur from the film. All other elements were below AES detection limits. (b) SIMS depth profiles for a 300 ± 30 nm thick pyrite film on Mo-coated glass. Raw ion fluxes for the matrix elements S, Mo, and Si are shown on a logarithmic scale in the upper graph. Atomic concentrations of C, H, O, Na, K, Al, Mg, and Ca appear in the lower graph. The dashed black line is the atomic density of pure pyrite (7.5×10^{22} atoms cm^{-3}). (c) SIMS depth profile for a 300 ± 30 nm thick pyrite film on a Mo-coated silicon substrate. Upper and lower graphs show matrix and impurity elements, respectively. The sample can be described as FeS_2/ $MoO_{0.1}S_{1.9}/MoO_{0.45}S_{1.55}/MoO_x$/Mo/Si. All impurity elements fell to their detection limits (DLs) upon sputtering into the undoped silicon substrate (estimated DLs: Na, K, Al, Mg: 2×10^{15}; Ca: 5×10^{15}; C: 2×10^{18}; O: 1×10^{19}; H: 2×10^{17} atoms cm^{-3}). Memory effects prevented lower DLs for C, H, and O. A comparison of the two SIMS profiles can be used to deduce the origin of the various impurities (see text).

$Fe(acac)_3$ ink rather than CVD (Table 2). These differences are caused by baking the $Fe(acac)_3$ ink layer in an oxidizing environment (air), which efficiently combusts the organics (yielding low C and H) but produces oxides (high O). In contrast, our CVD synthesis utilizes a reducing environment (the reaction of $Fe(acac)_3$ and *tert*-butyldisulfide in argon at 300 °C) that minimizes oxygen incorporation but is less effective at removing C and H from the films. Subsequent annealing of the films in H_2S and sulfur (for ink-made films) or sulfur only (CVD films) is apparently unable to erase the initial differences in impurity content inherited from the first steps of film processing. We note that the concentration of alkalis (K and Na) is ~4 times higher in the ink-made films and speculate that the extended annealing times used to fabricate these films result in greater alkali diffusion from the glass.

dx.doi.org/10.1021/ja311974n | J. Am. Chem. Soc. 2013, 135, 4412−4424

Table 2. Impurity Content of Pyrite Films Made via $Fe(acac)_3$ Ink vs CVD[a]

impurity	$Fe(acac)_3$ Mo/glass (ppm)	CVD[4] Mo/glass (ppm)	$Fe(acac)_3$ Mo/Si (ppm)
oxygen	8800	400	1750
potassium	3800	1000	50
sodium	1400	400	165
carbon	500	4000	900
hydrogen	340	2500	20−100
aluminum	160	100	165
calcium	10	20	2−6
magnesium	<1	20	<1

[a]Films on Mo-coated glass used identical substrates provided by a collaborator, while the Mo-coated Si substrate was prepared using an in-house sputter tool.

To determine the origin of the various impurities in the pyrite film on Mo-coated glass, we compare the SIMS depth profile of this film with data for a 300 ± 30 nm thick film made on a Mo-coated, undoped silicon substrate (Figure 5c). The Mo interlayer was necessary to grow high-quality, uniform pyrite films on the silicon substrates. Because the *i*-Si substrate is extremely pure, even by SIMS standards, it cannot be a source of any impurity other than Si itself. Indeed, the concentrations of all measured impurities fell below their SIMS detection limits after sputtering several hundred nanometers into the Si substrate (lower graph in Figure 5c). An analysis of the S, Mo, O, and Si depth profiles suggest that this film can be described as a $FeS_2/MoO_{0.1}S_{1.9}/MoO_{0.45}S_{1.55}/MoO_x/Mo/Si$ stack. Of the elements monitored by SIMS, we find that K and Na are present in much lower concentrations and O and H in somewhat lower concentrations in the pyrite film on the Mo-coated Si substrate (Table 2), while the levels of the other elements in the two films are equal within experimental error. The much lower level of alkalis in the film on Mo-coated Si indicates that leaching from glass is the principal source of alkali contamination in the pyrite layer grown on Mo-coated glass, as expected. However, K and Na are still present in substantial amounts (50 and 165 ppm) in the glass-free Si sample. Possible secondary sources of alkalis include the $Fe(acac)_3$ ink and the sputtered Mo layer. Of the three ink components, $Fe(acac)_3$ and sulfur contain very little alkalis (2.9 ppm Na and <0.1 ppm K according to the $Fe(acac)_3$ manufacturer; see Figure S6, Supporting Information) and cannot be the source of the contamination. Although the purity of the pyridine solvent is unknown, we believe that the Mo layer is the main source of alkalis in the film on Mo-coated silicon. The Mo was sputtered in-house from a 99.95% Mo target with 20 ppm of Na and 30 ppm of K (Figure S7, Supporting Information) and could account for the measured alkalis after diffusing throughout the film during air baking and annealing. The SIMS profiles show that this Mo layer is also heavily contaminated with oxygen and carbon compared to the Mo layers on glass substrates (which were supplied by a commercial manufacturer and undoubtedly feature higher purity and density), probably due to contamination of the argon process gas by air. Morphological differences between the commercial and homemade Mo layers may result in a less dense pyrite layer on the Mo-coated silicon and explain the lower O and H content of these films. The shape of the aluminum profile shows that Al is from the Fe(acac) ink, which is consistent with the relatively high concentration of Al in our $Fe(acac)_3$ starting material (30.5 ppm; Figure S6, Supporting Information). In summary, our SIMS data show that (i) pyrite films made from $Fe(acac)_3$ ink contain relatively large amounts of oxygen (0.2−0.9%) and small amounts of carbon and hydrogen, (ii) alkalis are

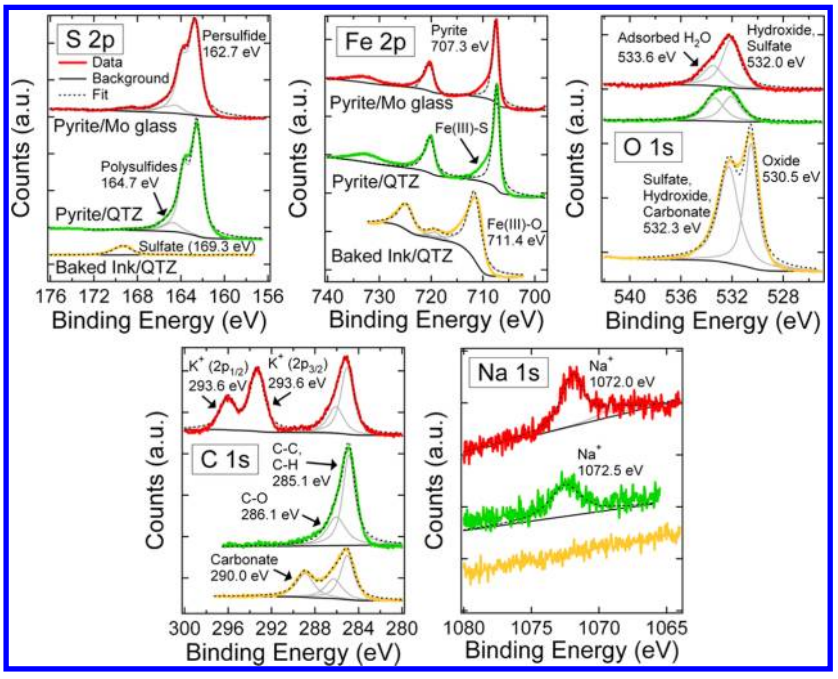

Figure 6. Surface composition by XPS. XP spectra of a sulfur-annealed pyrite film on a Mo-coated glass substrate (red plots), a sulfur-annealed pyrite film on a quartz substrate (green plots), and an air baked film of the $Fe(acac)_3$ ink on a quartz substrate (yellow plots). Sulfur-annealed samples were annealed in H_2S at 390 °C for 12 h followed by elemental sulfur at 550 °C for 8 h. Sulfur-annealed films were confirmed to be pure pyrite within the sensitivity of XRD and Raman spectroscopy. Sulfur-annealed films were exposed to air for ∼1 min as they were introduced into the XPS chamber. Air-baked films were prepared by spin-casting onto a quartz substrate followed by baking in air at 320 °C. Film thicknesses: 300 nm.

dx.doi.org/10.1021/ja311974n | *J. Am. Chem. Soc.* 2013, 135, 4412−4424

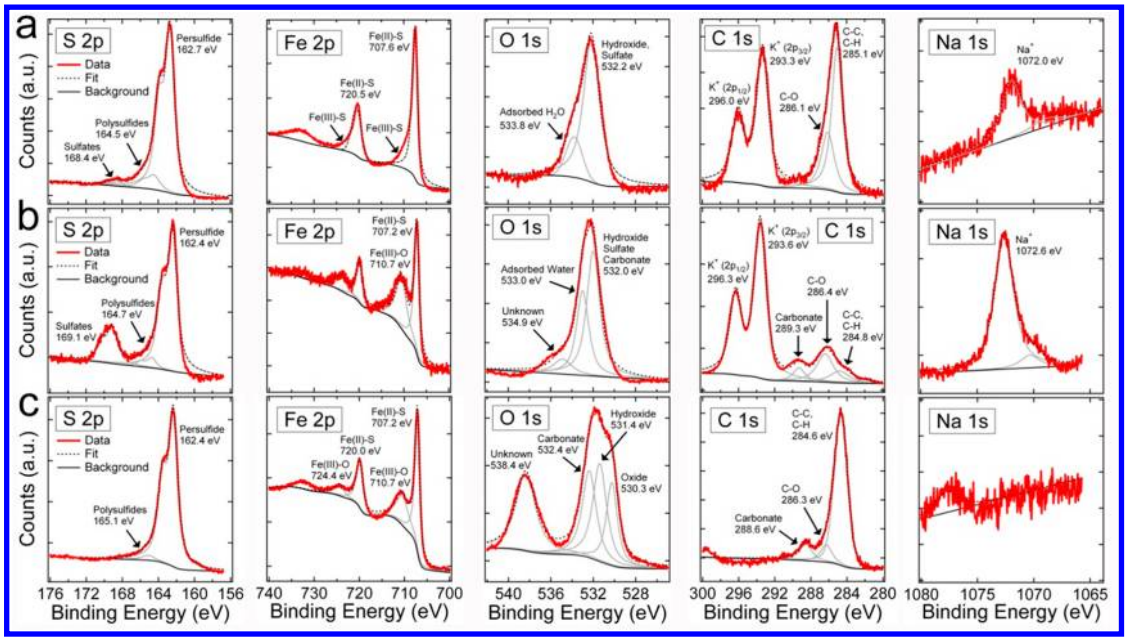

Figure 7. XP spectra of a sulfur-annealed pyrite film on a Mo-coated glass substrate (a) freshly prepared, (b) exposed to air for 10 h, and then (c) rinsed in deionized water for 10 s.

exogenous impurities leached from the glass substrate or molybdenum layer, and (iii) aluminum comes from the ink. Other elements are undoubtedly present in the pyrite layers at concentrations that could affect the electronic properties of these films. Ongoing work is directed at minimizing the load of electronically active impurities as a prerequisite for achieving rational control of the electronic characteristics of pyrite thin films.

XPS was used to determine the elemental composition of the surface of sulfur-annealed pyrite films on quartz and Mo-coated glass substrates as well as an air-baked ink layer on a quartz substrate. Figure 6 shows Fe 2p, S 2p, O 1s, C 1s, K 2p, and Na 1s spectra for these three films. Spectra of pyrite films on Mo-coated glass and quartz are very similar, differing mainly in the absence of K signal from films on quartz, so we describe only the films on Mo-coated glass here.

Fe 2p spectra of the pyrite films on Mo-coated glass are dominated by pyrite peaks ($2p^3/_2$ at 707.3 eV and $2p^1/_2$ at 720.2 eV).[41] Both of these peaks shows high-energy tails that are thought to be caused by slight Fe(III)−S or perhaps Fe(III)−O contamination of the surface, which has been observed even on single crystals cleaved in UHV as a result of spontaneous oxidation of Fe(II) to form surface monosulfide, S^{2-}.[42] Otherwise the Fe 2p spectra are clean and show no sign of additional iron species.

S 2p spectra show three sulfur species, each of which is fit as a doublet with a spin−orbit splitting of 1.2 eV: pyrite lattice persulfide (S_2^{2-}) with a $2p^3/_2$ binding energy of 162.7 eV; polysulfides (S_n^{2-}), which are a mixture of molecules deposited as a residue during sulfur annealing, at 164.5 eV; and sulfates (SO_4^{2-}) at 168.5 eV, which we believe are produced during brief exposure of the sample to air while loading the XPS chamber (<1 min).

O 1s spectra show a broad peak at 532.0 eV with a shoulder at higher energy. These spectra fit well with two peaks: one at 532.0 eV, attributed to a mixture of KOH, NaOH, and sulfates, and a second at 533.6 eV, which is characteristic of adsorbed water. In general, O 1s binding energies are 529.3−530.5 eV for oxide (O^{2-}), 531.4−532.0 eV for hydroxide (OH^-), and 533−534 eV for adsorbed H_2O.[43−45] The absence of an O^{2-} peak indicates that oxides are not present on the film surface in detectable concentrations.

The C 1s spectra contain both carbon and potassium peaks. The C 1s feature is a peak with a shoulder at high energy. It is fit well by peaks at 285.1 eV (C−C and C−H) and 286.1 eV (C−O) due to the adsorption of adventitious hydrocarbons and alcohols onto the film surface. Relatively large K 2p peaks at 293.3 and 296.0 eV (~2:1 intensity ratio, spin−orbit splitting of 2.7 eV) indicate a substantial amount of one or more potassium compounds on the film surface, which could include potassium sulfides (K_2S, KS, K_2S_3, KS_2, K_2S_5, or KS_3), oxides (K_2O, KO, or KO_2), and/or hydrolysis products such as KSH, KOH, KOOH, and so on.[46] Some sodium species are also present (Na 1s peak at ~1072.0 eV, consistent with Na_xS_y, NSH, NaOH, etc.).[47] We can rule out metallic K, for which the K 2p peaks would appear at 294.4 and 297.1 eV.[48] We can also rule out metallic Na based on the position of the Na $KL_{23}L_{23}$ Auger peak at 496.5 eV (metallic Na appears at 492 eV, data not shown).[49] The presence of alkali oxides and oxyhydroxides is ruled out based on the absence of an O^{2-} peak at 529.8 ± 0.4 eV.[47,50] We conclude that K and Na are present as a mixture of hydroxides and various S-containing species (sulfides, hydroxysulfides, sulfates). Sulfur in K_2S and Na_2S, found at 162.0 eV, could easily be present but would be obscured by the large persulfide peak.[51] Oxygen in KOH, NaOH, and Na_2SO_4 is found at 532.3 ± 0.4 eV[51,52,47,53] and accounts for the principal XP peak in our O 1s spectra. Both of these alkali metal ions diffuse into the pyrite film from the glass substrate during annealing and segregate at the film surface as sulfides. Upon brief exposure to air, the sulfides rapidly hydrolyze to produce KOH, NaOH, and small amounts of sulfates. The absence of oxidized iron species suggests that pyrite itself is not oxidized by brief air exposure. Rather, the alkali sulfide surface contamination is rapidly hydrolyzed in air. This surface contamination may act to protect the underlying pyrite from rapid chemical attack. We note that the alkali compounds are

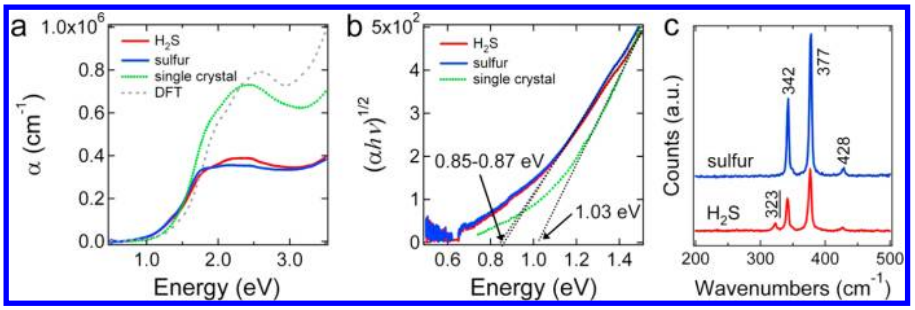

Figure 8. Optical properties. (a) Absorption coefficient across the solar spectrum (0.5−3.5 eV) for FeS_2 films before and after sulfur annealing (500 °C for 8 h). Data from a pyrite single crystal and a DFT model of bulk pyrite are shown for reference.[60] The natural single crystal had a room-temperature electron density of 1×10^{17} cm^{-3} and a mobility of 68 cm^2 V^{-1} s^{-1} as measured by the Hall effect. (b) A plot of $(\alpha h\nu)^{1/2}$ vs $h\nu$ showing an estimated allowed indirect bandgap of 0.85−0.87 ± 0.05 eV for the films and 1.03 ± 0.05 eV for the single crystal (dotted lines). (c) Raman spectra of the two films. The small marcasite impurity (323 cm^{-1}) is eliminated by sulfur annealing.

easily removed from the surface by rinsing with water (vide infra), which may be relevant for solar cell manufacturing (for example, during CBD deposition of window layers).

Compared to the film on Mo-coated glass, the film made on quartz lacks a potassium signal at 293−296 eV and has noticeably less sulfate both in the S 2p and O 1s spectra, probably as a result of much less alkali sulfide contamination on the film surface. Surprisingly, the film on quartz shows a small Na peak at 1072.5 eV. This Na peak is not present in the baked ink, apparently because the processing conditions (320 °C for 30 min) are too mild for sodium to diffuse to the substrate surface. During H_2S or sulfur annealing, however, sodium appears on the surface; we observed Na by XPS even on bare quartz substrates after H_2S annealing. In all other ways, the two sulfur-annealed films appear nearly identical in their surface composition.

In order to investigate the surface chemistry of the pyrite films in more detail, we remeasured the film on Mo-coated glass after exposing it to air (Figure 7b) and again after rinsing it in water (Figure 7c). Spectra from the fresh film are reproduced in Figure 7a. Exposure of the pyrite film to ambient laboratory air for 10 h results in significant changes to the data, including large increases in K, Na, O, and sulfate signals as well as the appearance of a broad oxidized iron signal centered at 710.7 eV. On the basis of the Fe $2p^3/_2$ peak position and the absence of O^{2-} in the oxygen spectrum, we can assign this oxidized iron species as some combination of $Fe(OH)_3$,[43,54,55] $FeSO_4$ (Fe $2p^3/_2$ = 711.3 eV, O 1s = 532.5 eV),[56] or $FeCO_3$ (Fe $2p^3/_2$ = 710.2 eV, C 1s = 289.4 eV, and O 1s = 531.9 eV),[57] but probably not $Fe(OH)_2$ (Fe $2p^3/_2$ = 709.5 eV) or $Fe_2(SO_4)_3$ (Fe $2p^3/_2$ = 713.5 eV).[56] The lack of an O^{2-} peak at 529.8 ± 0.4 eV indicates that oxides and oxyhydroxides such as hematite (α-Fe_2O_3), goethite (α-FeOOH), lepidocrocite (γ-FeOOH), maghemite (γ-Fe_2O_3), and magnetite (Fe_3O_4) are not formed in detectable quantities in this experiment.

The major change in the S 2p spectrum after air exposure is a significant increase in sulfate (169.1 eV) relative to persulfide and polysulfide, consistent with formation of $FeSO_4$ and accumulation of alkali sulfates. The O 1s spectrum shows a substantial increase in peak intensity, but the shape of the spectrum is largely unchanged except for the appearance of a pronounced shoulder at high energy (534.9 eV), which we are unable to assign at present. The main oxygen peak centered at 532.4 eV is composed of an admixture of hydroxide, sulfate, and carbonate (at 532.0 eV) and adsorbed water (at 533.0 eV). Changes in the C 1s spectrum include the growth of the C−O signal at 286.4 eV and the appearance of carbonate (CO_3^{2-}) at 289.3 eV, which may represent $FeCO_3$ or alkali carbonates. The adventitious carbon peak at 284.8 eV is significantly smaller than the other carbon peaks after air exposure.

The most striking effect of air exposure is the large increase in K and Na signals. We believe that air exposure induces the diffusion of alkali ions along grain boundaries and their accumulation at the hydrated surface of the film. Alkali ions (particularly sodium) are known to be mobile in polycrystalline chalcogenide films even at room temperature.[49,58] Evidently, potassium is also very mobile in our films. Taken together, these XPS data support a picture in which a subnanometer thick film of hydrated alkali and iron hydroxides, sulfates, and carbonates builds up on the pyrite surface over the first 10 h of air exposure. These species may exist as islands on the pyrite surface rather than as a continuous layer.

After XPS measurement, the oxidized pyrite film was immersed in deionized water for 10 s, dried, and measured again. As Figure 7c shows, the water rinse completely removes the K, Na, and sulfate species from the film surface, as expected for these highly soluble species. Yet, the oxidized iron (710.7 eV) persists. The appearance of O^{2-} (530.3 eV) and continued presence of OH^- (531.4 eV) suggests that some of the oxidized iron is FeOOH. It is likely that a mixture of iron oxides (e.g., amorphous Fe_2O_3), oxyhydroxides, and hydroxides covers the pyrite surface. Each of these iron species is quite insoluble in deionized water, so they may form either during the water rinse or in the time required to dry the film and load it into the XPS chamber. In addition, the clear presence of carbonate on the rinsed film (C 1s at 288.6 eV and O 1s at 532.4 eV) indicates that some fraction of the oxidized iron is $FeCO_3$. The origin of the broad peak at 538.4 eV in the O 1s spectrum is unclear.

Here, we have studied the effect of a water rinse only for films that have built up a layer of oxidized surface contamination over many hours of air exposure. In the future, it will be interesting to determine if water rinsing of fresh films can remove alkali and sulfate contaminants without leaving behind oxidized iron species on the film surface.

These analyses of the oxidized and water-washed pyrite films allow us to interpret the XPS data of the air-baked $Fe(acac)_3$ ink layer (orange spectra in Figure 6) as showing a mixture of iron(III) oxides, sulfate, and carbonate.[59] FeOOH may also be present. All of the original elemental sulfur has been oxidized or evaporated from the film surface. Although we have not performed depth profiling measurements to analyze the film

dx.doi.org/10.1021/ja311974n | J. Am. Chem. Soc. 2013, 135, 4412−4424

bulk, we believe that the surface composition is representative of the entire thickness of the air baked film. XRD shows that the film is amorphous. As mentioned above, we conclude that the baked ink layer is a mixture of amorphous iron oxides, oxyhydroxide, hydroxysulfates, sulfate ($Fe_2(SO_4)_3$), and carbonate ($Fe_2(CO_3)_3$) species.

Optical Properties of Pyrite Films. The optical absorption coefficient (α) and optical band gap (E_g) of FeS_2 films on quartz substrates were determined from transmittance and reflectance measurements using an integrating sphere. Films were measured before and after sulfur annealing in order to determine the effect of the small marcasite impurity (<10 vol %) on the optical properties of the mixed-phase films. Figure 8a,b shows that α and E_g are essentially unchanged by sulfur annealing despite full conversion of marcasite to pyrite (Figure 8c). In both films, α reaches a value of 7×10^4 cm^{-1} at $h\nu$ = 1.25 eV (α^{-1} = 143 nm) and levels off at 3.4−3.9 $\times 10^5$ cm^{-1} for $h\nu$ > 1.75 eV (α^{-1} < 29 nm), while the band gaps fit well to allowed indirect transitions with E_g = 0.85−0.87 ± 0.05 eV. Figure 8a compares the film data with recent results for a pyrite single crystal measured by spectroscopic ellipsometry as well as a DFT model of bulk pyrite.[60] While the shape of all four curves is similar, α of the films is about half as large as that of the single crystals for $h\nu$ > 2 eV because voids and surface roughness in the films result in an overestimation of the effective film thickness. We believe that fully dense and flat films would yield α values similar to those of the single crystals (i.e., α^{-1} < 15 nm for $h\nu$ > 2 eV). It is important to note that the band gap of these films is 0.1−0.15 eV smaller than the gaps measured for single crystals (Figure 8b) or pyrite films grown by CVD (see ref 4 and the marcasite band gap discussion below). The ink-made films also show a softer band edge (i.e., a more pronounced subgap absorption tail) than the CVD films (vide infra). The most likely cause of the smaller band gap and more extended subgap absorption tail is greater structural disorder and higher defect concentrations in our $Fe(acac)_3$-made films, possibly as a result of producing pyrite via sulfurization of amorphous iron oxides/salts rather than "direct" synthesis of crystalline pyrite by CVD.

Optical Properties and Band Gap of Marcasite. The fact that a substantial marcasite impurity is invisible in the optical absorption spectra of our mixed-phase films raises renewed questions about the band gap and optical functions of marcasite. Marcasite is thought to have a band gap of ∼0.34 eV, which would make it unsuitable for solar energy conversion in bulk form and a deleterious phase impurity in pyrite.[61] Sun et al. recently challenged this notion by presenting rigorous DFT calculations indicating that marcasite probably has a *larger* band gap than pyrite.[62] These authors pointed out that the purported value of the marcasite gap is based on variable-temperature resistivity data from a single natural marcasite crystal published in 1980.[63] Fitting of resistivity data is an unreliable way to determine the band gap of a semiconductor of unknown purity and carrier mobility and should be verified with additional techniques. We confirmed the results of Sun et al. using our own DFT calculations of marcasite, finding the band gaps of marcasite and pyrite to be 0.79 and 0.63 eV, respectively, at the generalized gradient approximation (GGA) level of theory (see the Supporting Information for details on the DFT-derived band structure and optical functions of marcasite). Our mixed-phase marcasite/pyrite thin films provide an opportunity to test these DFT predictions against experimental data.

Definitive measurements of the optical properties of marcasite requires the growth of thin films with significantly more marcasite content than has been possible using our $Fe(acac)_3$ ink route. Although we cannot yet make phase-pure marcasite films by any method (see above), we can make optically transparent FeS_2 films that are ∼50 vol % marcasite via CVD growth on sodium-free substrates such as quartz.[4] Phase quantification was performed using XRD pattern analysis (see the Methods section). The as-grown CVD films show large marcasite peaks in both XRD and Raman data (red plots in Figure 9a,b). Careful sulfur annealing of these films converts

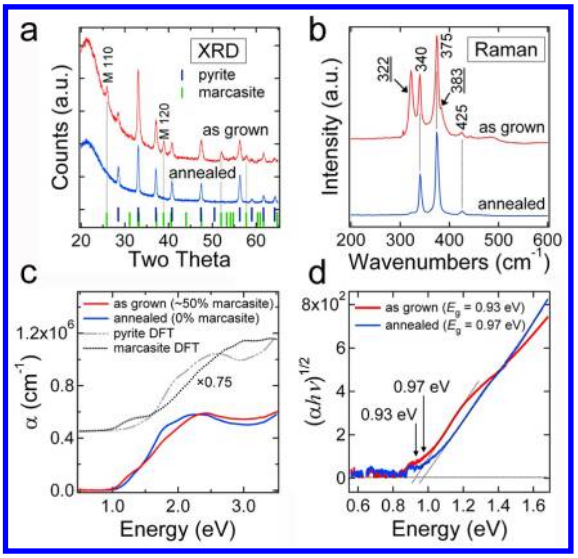

Figure 9. Marcasite optical properties. (a) XRD patterns and (b) Raman spectra of a representative 85 ± 17 nm thick CVD FeS_2 film before and after sulfur annealing. As-grown films contain ∼50 vol % marcasite. Annealing completely converts marcasite to pyrite. Underlined labels indicate marcasite peaks. (c) Absorptivity spectra of the as-grown film (red) and annealed film (blue), as well as calculated spectra for pyrite (gray hashes) and marcasite (black dots). The marcasite spectrum is the average of the optical functions along the [100], [010], and [001] directions of the orthorhombic crystal. The calculated spectra are scaled by a factor of 0.75 and offset for clarity. See Figure S8 (Supporting Information) for the experimental data plotted on a semilog scale. (d) Plot of $(\alpha h\nu)^{1/2}$ versus energy used to estimate the band gap of the two films.

marcasite to pyrite, yielding phase-pure pyrite films while avoiding significant changes to film microstructure that would complicate spectral comparisons (blue plots in Figure 9a,b). Optical measurements of the films before and after annealing show only subtle differences in absorptivity spectra and estimated optical band gap (Figure 9c,d). The main differences are as follows: (i) mixed-phase films may have a slightly smaller band gap than phase-pure pyrite films (0.93 vs 0.97 eV); (ii) mixed-phase films feature a small shoulder at ∼1.25 eV, absent in phase-pure films; (iii) mixed-phase films have a more gradual increase in absorption coefficient; (iv) phase-pure films show a more pronounced dip in absorptivity at ∼3 eV. The spectra of both types of films plateau at $\alpha \sim 5.5 \times 10^5$ cm^{-1} for photon energies above 2−2.25 eV. These data provide strong evidence that the optical band gap of marcasite is *at least* as large as that of pyrite, contrary to previous belief[63,61] and in agreement with recent DFT calculations.[62] Furthermore, the absorptivity

dx.doi.org/10.1021/ja311974n | J. Am. Chem. Soc. 2013, 135, 4412−4424

spectra of the two polymorphs appear to be quite similar across the solar window.

Our conclusions are further strengthened by the excellent agreement between experimental and computed absorptivity spectra (Figure 9c). Calculated absorptivity spectra of pyrite and marcasite were derived from their respective optical functions as determined by DFT (see ref 60 and the Supporting Information). Remarkably, the calculated spectra capture all of the subtle differences in the experimental data, including the shoulder at ~1.25 eV, the steeper absorption rise for pyrite, and the dip in absorptivity at ~3 eV. The calculated spectra also plateau at a similar α value for both polymorphs, in agreement with experiment (note, however, that $\alpha_{calculated} \sim 8-9 \times 10^5$ cm^{-1} but $\alpha_{experimental} \sim 5.5 \times 10^5$ cm^{-1}, suggesting that the thin films contain voids, as mentioned above for the ink-made films). We emphasize that this comparison between experiment and theory was carried out using a "double-blind" approach in which, to avoid bias, neither the theoretician nor the experimentalist knew of each other's results beforehand. The excellent agreement between the spectra validates the accuracy of recent DFT models for both marcasite and pyrite. We conclude that the marcasite electronic and optical band gaps are at least as large as those of pyrite. Rather than being inherently unsuitable for solar energy conversion, pure marcasite films, if they can be synthesized, may very well have better optical and electronic properties than pyrite itself.

However, our results do not imply that marcasite is necessarily a benign impurity in pyrite. Although marcasite almost certainly has a larger gap than pyrite and similar absorptivity, the existence of band edge offsets and electronic defects at the pyrite/marcasite interface as well as other types of disorder may result in degraded electronic properties for mixed-phase pyrite/marcasite thin films. We therefore continue to believe that the synthesis of phase-pure films, whether pyrite or marcasite, remains desirable for solar energy applications.

Electrical Properties. The electrical properties of FeS_2 films on quartz substrates were assessed by variable-temperature Hall effect measurements (80–350 K) in a van der Pauw geometry with ohmic contacts made to the samples by evaporated silver pads and gold-coated copper pins. Three sulfur-annealed, phase-pure pyrite films and four H_2S-annealed, mixed-phase films were studied. The in-plane Hall mobility of all films is too low to be measured (<1 cm^2 V^{-1} s^{-1}), which also prevents determination of the carrier type from the sign of the Hall voltage. However, qualitative thermopower measurements indicate that all of the films are p-type. The dark resistivity before and after sulfur annealing is 0.65 ± 0.10 and 1.9 ± 0.83 Ω cm at room temperature and 15 ± 4.5 and 38 ± 24 Ω cm at 80 K, respectively (Figure 10). Arrhenius plots of the resistivity are curved downward. The resistivity of each film shows a temperature dependence of the form $\rho = \rho_0 \exp[(T_0/T)^a]$ with $a \approx 0.5$ (inset in Figure 10). Using $a = 0.5$ gives $\rho_0 = 0.0236$ and 0.0576 Ω cm and $T_0 = 3188$ and 2899 K for the films before and after sulfur annealing. The logarithmic derivative analysis employed by Baruth et al.[64] yields $a = 0.59$ and 0.62 for these two films. Best fits to $\rho = \rho_0 \exp[(T_0/T)^a]$ for the seven ink-made films give similar values to films grown by CVD[4] and reactive sputtering[64] (see Figure S12a and Table S2, Supporting Information). A temperature-dependent resistivity with $a \approx 0.5$ is often interpreted as evidence of Efros–Shklovskii variable range hopping (ES-VRH) transport.[65] However, the curved Arrhenius data can be fit equally well by other models, such as the model proposed by Werner that considers transport in polycrystalline films to be limited by thermionic emission across inhomogeneous grain boundaries with a Gaussian distribution of barrier heights.[66] Resistivity in the Werner model is given by

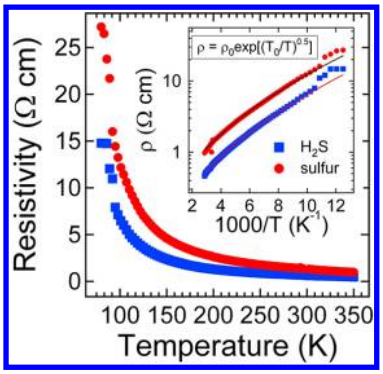

Figure 10. Electrical resistivity of pyrite and mixed-phase FeS_2 films. Resistivity as a function of temperature (80–350 K) for representative 320 nm thick films on quartz substrates before sulfur annealing (blue squares) and after sulfur annealing (red circles). The room-temperature resistivity of the two films is 0.64 and 1.35 Ω cm, respectively. Inset is a log–linear plot of the resistivity versus inverse temperature. The data are nonlinear and fit well to $\rho = \rho_0 \exp[(T_0/T)^a]$ with $a = 0.5$.

$$\rho = \rho_0 \exp\left[q\left(\Phi - \frac{{\sigma_\Phi}^2}{2kT/q} \right)/kT \right]$$

where Φ is the average barrier height and σ_Φ is the standard deviation of the barrier height. Fits to this model yield $\Phi = 40$ meV and $\sigma_\Phi = 12$ meV for films both before and after sulfur annealing. Remarkably, FeS_2 films show very similar resistivity curves and fit well to either model regardless of fabrication method (ink, CVD, or sputtering) and marcasite content (Figure S12, Supporting Information). Considering the limited data available, there is little justification for choosing any particular model over another. Further studies over a wider temperature range are necessary to determine the mechanisms of carrier transport in these polycrystalline FeS_2 films.

The fact that nearly all unintentionally doped pyrite thin films have essentially the same electrical properties (i.e., high conductivity, low mobility, weakly activated p-type transport characteristic of a highly doped but nondegenerate semiconductor)[67–78] regardless of stoichiometry and fabrication method implies that a single robust bulk or surface effect dominates the electrical behavior of these films. As we recently summarized,[4] possible explanations for the universal behavior of pyrite films include the presence of the following: (i) a ubiquitous extrinsic dopant, for example, oxygen;[79] (ii) nanoscale phase impurities, especially amorphous domains;[80] (iii) surface effects, particularly a hole accumulation or inversion layer.[81] Ongoing studies of synthetic pyrite single crystals in our laboratories are aiding the evaluation of these three possibilities.[82] In stark contrast to the pyrite films, our nominally undoped pyrite single crystals are n-type, with room-temperature electron concentrations of 10^{15}–10^{16} cm^{-3}, mobilities of 200–400 cm^2 V^{-1} s^{-1}, and activation energies of ~200 meV. We now briefly assess the three explanations mentioned above in light of our initial comparisons between the films and single crystals:

Ubiquitous Dopant Such as Oxygen. It is possible that pyrite films show very similar electrical properties because they

dx.doi.org/10.1021/ja311974n | J. Am. Chem. Soc. 2013, 135, 4412–4424

contain a common dopant. The identity of the alleged dopant is an open question. Native defects appear to be ruled out based on both the lack of a correlation between the iron-to-sulfur ratio and electrical properties[4] as well as recent calculations showing that native defects should exist only in negligible concentration in bulk pyrite and probably cannot account for the large carrier densities observed in pyrite films.[80,79,83] Non-native defects such as substitutional oxygen or interstitial hydrogen are more plausible universal dopants in pyrite films. However, the single crystals and thin films made in our laboratories show similar levels of oxygen, hydrogen, and carbon via elemental analysis, yet the single crystals are n-type, not p-type, and have orders of magnitude lower carrier concentration than the films. Thus, we tentatively conclude that a ubiquitous dopant such as oxygen is not responsible for the universal electrical properties of pyrite films. However, we caution that more complicated defect associations and clusters may be present in films but absent in single crystals (due to the different processing conditions) and could in principle explain the distinct behavior of these two types of pyrite samples.

Nanoscale Amorphous Impurities. It is probably impossible to rule out the presence of nanoscale amorphous impurities in pyrite films using only XRD, Raman spectroscopy, and magnetic measurements. Such impurities may exist as a result of imperfect crystallization due to the relatively low processing temperatures and complicated carbon-containing precursors used to make the films. Perhaps single crystals show much different electrical behavior because they are made from the elements at higher temperatures and therefore lack the amorphous domains that plague the films. The absence of amorphous regions in single crystals would also explain why photoelectrochemical[1] and Schottky[2] solar cells based on single crystals can achieve very high external quantum efficiency, whereas films are so far not photoactive. The excellent electrical properties of our single crystals show that phase impurities are not inevitable in pyrite, if indeed they are present at all in properly made pyrite films. High-resolution transmission electron microscopy studies will be useful to search for amorphous domains and other defects in high-quality, sectioned pyrite films.

Hole Accumulation/Inversion Layer. Pyrite films may be heavily hole doped and highly conductive because of a hole-rich layer that forms at the crystal surface (accumulation layer in p-type material or inversion layer in n-type material). Surface accumulation/inversion layers are well known in semiconductors such as HgCdTe[84] and InN[85,86] and if persistent can dominate the electrical properties of these materials. Using a combination of the Hall effect and UV photoelectron spectroscopy measurements, Bronold et al. deduced that a surface hole inversion layer is present on n-type pyrite single crystals.[81] The hole inversion layer is believed to result from a large concentration of surface states located near the valence band edge. Our own Hall effect data on single crystals are consistent with the coexistence of an n-type bulk layer and a p-type surface layer.[82] For geometric reasons, surface effects are more severe in polycrystalline thin films than single crystals, and it is easy to envision a hole-rich surface layer controlling charge transport in pyrite films. Chemical passivation of the alleged surface states could eliminate this surface layer and enable more rational control of the electrical behavior of pyrite films for solar cells.

CONCLUSIONS

Phase-pure, polycrystalline iron pyrite thin films have been fabricated by solution-phase deposition of an $Fe(acac)_3$/sulfur ink followed by sequential annealing in air, H_2S, and sulfur gas at temperatures ranging from 320 to 550 °C. FTIR and XPS data show that the acetylacetonate ink layer is first converted to a mixture of iron oxides, hydroxides, sulfates, and carbonates by air annealing and then sulfurized to form pyrite. The sulfur-annealed films are pure-phase pyrite to within the detection limit of synchrotron XRD and Raman spectroscopy. Films on Mo-coated glass substrates consist of densely packed columnar grains and are uniform in thickness (±5%), fairly smooth (RMS roughness on the order of 10% of the film thickness), free of cracks and pinholes, and mechanically adherent and robust. These films can be described as $FeS_2/MoO_{0.03}S_{1.97}/MoO_xS_{2-x}$/glass stacks (with $x > 0.03$). SIMS shows that the total impurity load in the pyrite layers of these films is ∼1.5 atom %, with a ∼20-fold larger concentration of oxygen but ∼7-fold smaller amounts of carbon and hydrogen than similar films produced by CVD. Detailed XPS data show that (i) potassium and sodium accumulate on the film surface, (ii) air exposure results in the slow buildup of a layer of hydrated alkali and iron hydroxides, sulfates, and carbonates, and (iii) rinsing the oxidized films in water completely removes the alkali and sulfate contaminants but not the insoluble oxidized iron species. Films grown on quartz substrates have an indirect optical band gap of 0.87 ± 0.05 eV, which is 0.1−0.15 eV smaller than that of CVD and single-crystal samples, perhaps reflecting greater structural disorder and higher defect concentrations in the solution-deposited films. Optical measurements of marcasite-rich samples indicate that marcasite has a band gap at least as large as that of pyrite and that the two polymorphs share similar absorptivity spectra, in excellent agreement with DFT results. The in-plane electrical properties of these films are qualitatively identical to nearly all other unintentionally doped FeS_2 samples in the literature: regardless of the marcasite content and impurity load, the films show p-type, weakly activated transport with a curved Arrhenius plot, a room-temperature resistivity of ∼1 Ω cm, and a hole mobility that is too small to measure by the Hall effect. This universal electrical behavior strongly suggests that a common bulk or surface effect dominates transport in FeS_2 thin films. We outlined three possible explanations for this universal behavior, that is, a common dopant, nanoscale phase impurities, or a hole accumulation/inversion layer. Comparative studies with single crystals seem to rule out the common dopant hypothesis, while the other two possibilities are the focus of ongoing work in our laboratories.

ASSOCIATED CONTENT

Supporting Information

Additional UV−vis, XRD, and SEM data, certificates of analysis, and discussion of marcasite DFT modeling. This material is available free of charge via the Internet at http://pubs.acs.org.

AUTHOR INFORMATION

Corresponding Author

matt.law@uci.edu

Notes

The authors declare no competing financial interest.

■ ACKNOWLEDGMENTS

We acknowledge the NSF SOLAR Program (Award CHE-1035218) for support of this work. We thank Zachary Fisk for the use of his quartz tube sealing setup and Mohammed El Makkaoui for assistance with UV−vis spectroscopy. Use of the Advanced Photon Source at Argonne National Laboratory was supported by the U.S. Department of Energy, Office of Science, Office of Basic Energy Sciences, under contract no. DE-AC02-06CH11357. Density functional calculations were performed on NSF-XSEDE supercomputers. C.L.P. acknowledges support by the U.S. Department of Energy under contract no. DE-AC36-08-GO28308 with the National Renewable Energy Laboratory.

■ REFERENCES

(1) Ennaoui, A.; Fiechter, S.; Jaegermann, W.; Tributsch, H. *J. Electrochem. Soc.* **1986**, *133*, 97.
(2) Büker, K.; Alonso-Vante, N.; Tributsch, H. *J. Appl. Phys.* **1992**, *72*, 5721.
(3) Ennaoui, A.; Fiechter, S.; Pettenkofer, C.; Alonso-Vante, N.; Buker, K.; Bronold, M.; Höpfner, C.; Tributsch, H. *Sol. Energy Mater. Sol. Cells* **1993**, *29*, 289.
(4) Berry, N.; Cheng, M.; Perkins, C. L.; Limpinsel, M.; Hemminger, J. C.; Law, M. *Adv. Energy Mater.* **2012**, *2*, 1124.
(5) Habas, S. E.; Platt, H. A. S.; van Hest, M. F. A. M.; Ginley, D. S. *Chem. Rev.* **2010**, *110*, 6571.
(6) Abass, A. K.; Ahmed, Z. A.; Tahib, R. E. *Phys. Status Solidi A* **1986**, *97*, 243.
(7) Smestad, G.; Da Silva, A.; Tributsch, H.; Fiechter, S.; Kunst, M.; Meziani, N.; Birkholz, M. *Sol. Energy Mater.* **1989**, *18*, 299.
(8) Smestad, G.; Ennaoui, A.; Fiechter, S.; Tributsch, H.; Kautek, W. *Solar Energy Mater.* **1990**, *20*, 149.
(9) Yamamoto, A.; Nakamura, M.; Seki, A.; Li, E. L.; Hashimoto, A.; Nakamura, S. *Sol. Energy Mater. Sol. Cells* **2003**, *75*, 451.
(10) Ouertani, B.; Ouerfelli, J.; Saadoun, M.; Bessais, B.; Ezzaouia, H.; Bernede, J. C. *Mater. Charact.* **2005**, *54*, 431.
(11) Arico, A. S.; Antonucci, V.; Anntonucci, P. L.; Modica, E.; Ferrara, S.; Giordano, N. *Mater. Lett.* **1992**, *13*, 12.
(12) Dong, Y.; Zheng, Y.; Duan, H.; Sun, Y.; Chen, Y. *Mater. Lett.* **2005**, *59*, 2398.
(13) Gomes, A.; Ares, J.; Ferrer, I.; Da Silva Pereira, M.; Sanchez, C. *Mater. Res. Bull.* **2003**, *38*, 1123.
(14) Nakamura, S.; Yamamoto, A. *Sol. Energy Mater. Sol. Cells* **2001**, *65*, 79.
(15) Li, E. L.; Seki, S.; Liu, F.-B.; Zheng, J.-B. *Semicond. Photonics Technol.* **2001**, *7*, 89.
(16) Pimenta, G.; Schröder, V.; Kautek, W. *Ber. Bunsen−Ges.* **1991**, *95*, 1470.
(17) Chatzitheodorou, G.; Fiechter, S.; Kunst, M.; Luck, J.; Tributsch, H. *Mater. Res. Bull.* **1988**, *23*, 1261.
(18) Prabukanthan, P.; Soukup, R. J.; Ianno, N. J.; Sarkar, A.; Kment, S.; Kmentova, H.; Kamler, C. A.; Exstrom, C. L.; Olejnicek, J.; Darveau, S. A. Chemical Bath Deposition (CBD) of Iron Sulfide Thin Films for Photovoltaic Applications, Crystallographic and Optical Properties, *Proceedings of the 35th Photovoltaics Specialists Conference*, Honolulu, HI, United States, June 20−25, 2010, Institute of Electrical and Electronics Engineers: Washington, DC, 2010; p 2965.
(19) Duan, H.; Zheng, Y. F.; Dong, Y. Z.; Zhang, X. G.; Sun, Y. F. *Mater. Res. Bull.* **2004**, *39*, 1861.
(20) Huang, L.; Wang, F.; Luan, Z.; Meng, L. *Mater. Lett.* **2010**, *64*, 2612.
(21) Wang, F.; Huang, L.; Luan, Z.; Huang, J.; Meng, L. *Mater. Chem. Phys.* **2012**, *132*, 505.
(22) Kment, S.; Kmentova, H.; Sarkar, A.; Soukup, R. J.; Ianno, N. J.; Krysa, J.; Hubicka, Z.; Olejnicek, J.; Exstrom, C. L.; Darveau, S. A. A Novel Sol−Gel Route to Pinhole-Free Iron Sulfide Thin Films, *Proceedings of the 37th Photovoltaics Specialists Conference*, Seattle, WA, United States, June 19−24, 2011, Institute of Electrical and Electronics Engineers: Washington, DC, 2010; p 1287.
(23) Willeke, G.; Blenk, O.; Kloc, Ch.; Bucher, E. *J. Alloys Compd.* **1992**, *178*, 181.
(24) Puthussery, J.; Seefeld, S.; Berry, N.; Gibbs, M.; Law, M. *J. Am. Chem. Soc.* **2011**, *133*, 716.
(25) Bi, Y.; Yuan, Y.; Exstrom, C. L.; Darveau, S. A.; Huang, J. *Nano Lett.* **2011**, *11*, 4953.
(26) Wang, D.-Y.; Jiang, Y.-T.; Lin, C.-C.; Li, S.-S.; Wang, Y.-T.; Chen, C.-C.; Chen, C.-W. *Adv. Mater.* **2012**, *24*, 3415.
(27) Li, W.; Döblinger, M.; Vaneski, A.; Rogach, A. L.; Jäckel, F.; Feldmann, J. *J. Mater. Chem.* **2011**, *21*, 17946.
(28) Kirkeminde, A.; Scott, R.; Ren, S. *Nanoscale* **2012**, *4*, 7649.
(29) Mitzi, D. B. *Adv. Mater.* **2009**, *21*, 3141.
(30) Liu, W.; Mitzi, D. B.; Yuan, M.; Kellock, A. J.; Chey, S. J.; Gunawan, O. *Chem. Mater.* **2010**, *22*, 1010.
(31) Todorov, T.; Mitzi, D. B. *Eur. J. Inorg. Chem.* **2010**, 17.
(32) Todorov, T. K.; Tang, J.; Santanu, B.; Gunawan, O.; Gokmen, T.; Zhu, Y.; Mitzi, D. B. *Adv. Energy Mater.* **2012**, *3*, 34.
(33) Weil, B. D.; Connor, S. T.; Cui, Y. *J. Am. Chem. Soc.* **2010**, *132*, 6642.
(34) Perkins, C. L.; Egaas, B.; Repins, I.; To, B. *Appl. Surf. Sci.* **2010**, *257*, 878.
(35) Briggs, D.; Seah, M. P. *Practical Surface Analysis*; Wiley: New York, 1990.
(36) Meyer, B. *Chem. Rev.* **1976**, *76*, 367.
(37) Vogt, H.; Chattopadhyay, T.; Stolz, H. J. *J. Phys. Chem. Solids* **1983**, *44*, 869.
(38) Sourisseau, C.; Cavagnat, R.; Fouassier, M. *J. Phys. Chem. Solids* **1991**, *52*, 537.
(39) White, S. N. *Chem. Geol.* **2009**, *259*, 240.
(40) Hu, J.; Zhang, Y.; Law, M.; Wu, R. *J. Am. Chem. Soc.* **2012**, *134*, 13216.
(41) Eggleston, C. M.; Ehrhardt, J.-J.; Stumm, W. *Am. Mineral.* **1996**, *81*, 1036.
(42) Nesbitt, H. W.; Muir, I. J. *Geochim. Cosmochim. Acta* **1994**, *58*, 4667.
(43) Haber, J.; Stoch, J.; Ungier, L. *J. Electron Spectrosc. Relat. Phenom.* **1976**, *9*, 459.
(44) Torres, J.; Perry, C. C.; Bransfield, S. J.; Fairbrother, D. H. *J. Phys. Chem. B* **2003**, *107*, 5558.
(45) Piras, F. M.; Rossi, A.; Spencer, N. D. *Tribol. Lett.* **2003**, *15*, 181.
(46) Moulder, J. F.; Stickle, W. F.; Sobol, P. E.; Bomben, K. D. In *Handbook of X-ray Photoelectron Spectroscopy*; Chastain, J., Ed.; Perkin Elmer: Eden Prairie, MN, 1992; pp 66−67.
(47) Barrie, A.; Street, F. J. *J. Electron Spectrosc. Relat. Phenom.* **1975**, *7*, 1.
(48) Li, S.; Kang, E. T.; Neoh, K. G.; Ma, Z. H.; Tan, K. L.; Huang, W. *Appl. Surf. Sci.* **2001**, *181*, 201.
(49) Niles, D. W.; Ramanathan, K.; Hasoon, F.; Noufi, R.; Tielsch, B. J.; Fulghum, J. E. *J. Vac. Sci. Technol., A* **1997**, *15*, 3044.
(50) Naumkin, A. V.; Kraut-Vass, A.; Gaarenstroom, S. W.; Powell, C. J. *NIST X-ray Photoelectron Spectroscopy Database*, version 3.5; National Institute of Standards and Technology: Gaithersburg, MD, 2003; http://srdata.nist.gov/xps/.
(51) Lindberg, B. J.; Hamrin, K.; Johansson, G.; Gelius, U.; Fahlman, A.; Nordling, C.; Siegbahn, K. *Phys. Scr.* **1970**, *1*, 286.
(52) Citrin, P. H. *Phys. Rev. B* **1973**, *8*, 5545.
(53) Kishi, K.; Ikeda, S. *Bull. Chem. Soc. Jpn.* **1973**, *46*, 341.
(54) Marcus, P.; Olefjord, I. *Corros. Sci.* **1988**, *28*, 589.
(55) McIntyre, N. S.; Zetaruk, D. G. *Anal. Chem.* **1977**, *49*, 1521.
(56) Brion, D. *Appl. Surf. Sci.* **1980**, *5*, 133.
(57) Heuer, J. K.; Stubbins, J. F. *Corros. Sci.* **1999**, *41*, 1231.
(58) Song, X.; Caballero, R.; Félix, R.; Gerlach, D.; Kaufmann, C. A.; Schock, H.-W.; Wilks, R. G.; Bär, M. *J. Appl. Phys.* **2012**, *111*, 034903.
(59) Biesinger, M. C.; Payne, B. P.; Grosvenor, A. P.; Lau, L. W. M.; Gerson, A. R.; Smart, S. T. C. *Appl. Surf. Sci.* **2011**, *257*, 2717.
(60) Choi, S. G.; Hu, J.; Abdallah, L. S.; Limpinsel, M.; Zhang, Y. N.; Zollner, S.; Wu, R. Q.; Law, M. *Phys. Rev. B* **2012**, *86*, 115207.

(61) Thomas, B.; Diesner, K.; Cibik, T.; Ellmer, K. *Solid State Phenom.* **1996**, *51*−*52*, 301.
(62) Sun, R.; Chan, M. K. Y.; Ceder, G. *Phys. Rev. B* **2011**, *83*, 235311.
(63) Jagadeesh, M. S.; Seehra, M. S. *Phys. Lett.* **1980**, *80A*, 59.
(64) Baruth, A.; Manno, M.; Narasimhan, D.; Shankar, A.; Zhang, X.; Johnson, M.; Aydil, E. S.; Leighton, C. *J. Appl. Phys.* **2012**, *112*, 054328.
(65) Shklovskii, B. I.; Efros, A. L. *Electronic Properties of Doped Semiconductors*; Springer: New York, 1984.
(66) Werner, J. H. *Solid State Phenom.* **1994**, *37*−*38*, 213.
(67) Thomas, B.; Höpfner, C.; Ellmer, K.; Fiechter, S.; Tributsch, H. *J. Cryst. Growth* **1995**, *146*, 630.
(68) Ares, J. R.; Ferrer, I. J.; Cuevas, F.; Sanchez, C. R. *Thin Solid Films* **2001**, *387*, 97.
(69) Wan, D. Y.; Wang, Y. T.; Wang, B. Y.; Ma, C. X.; Sun, H.; Wei, L. *J. Cryst. Growth* **2003**, *253*, 230.
(70) Lichtenberger, D.; Ellmer, K.; Schieck, R.; Fiechter, S.; Tributsch, H. *Thin Solid Films* **1994**, *246*, 6.
(71) Höpfner, C.; Ellmer, K.; Ennaoui, A.; Pettenkofer, C.; Fiechter, S.; Tributsch, H. *J. Cryst. Growth* **1995**, *151*, 325.
(72) Thomas, B.; Cibik, T.; Höpfner, C.; Diesner, K.; Ehlers, G.; Fiechter, S.; Ellmer, K. *J. Mater. Sci.: Mater. Electron.* **1998**, *9*, 61.
(73) Meester, B.; Reijnen, L.; Goossens, A.; Schoonman, J. *Chem. Vap. Deposition* **2000**, *6*, 121.
(74) Ellmer, K.; Lichtenberger, D.; Ennaoui, A.; Hopfner, C.; Fiechter, S.; Tributsch, H. Comparison of Structural, Optical and Electrical Properties of Pyrite (FeS_2) Layers Prepared by MOCVD (Normal and Low Pressure) and Reactive Magnetron Sputtering, *Proceedings of the 23rd Photovoltaics Specialists Conference*, Louisville, KY, United States, May 10−14, 1993, Institute of Electrical and Electronics Engineers: Washington, DC, 1993; p 535.
(75) Willeke, G.; Dasbach, R.; Sailer, B.; Bucher, E. *Thin Solid Films* **1992**, *213*, 271.
(76) Meng, L.; Liu, Y. H.; Tian, L. *J. Cryst. Growth* **2003**, *253*, 530.
(77) Hamdadou, N.; Khelil, A.; Bernede, J. C. *Mater. Chem. Phys.* **2003**, *78*, 591.
(78) Bronold, M.; Kubala, S.; Pettenkofer, C.; Jaegermann, W. *Thin Solid Films* **1997**, *304*, 178.
(79) Sun, R.; Chan, M. K. Y.; Kang, S. Y.; Ceder, G. *Phys. Rev. B* **2011**, *84*, 035212.
(80) Yu, L.; Lany, S.; Kykyneshi, R.; Jieratum, V.; Ravichandran, R.; Pelatt, B.; Altschul, E.; Platt, H. A. S.; Wager, J. F.; Keszler, D. A.; Zunger, A. *Adv. Energy Mater.* **2011**, *1*, 748.
(81) Bronold, M.; Pettenkofer, C.; Jaegermann, W. *J. Appl. Phys.* **1994**, *76*, 5800.
(82) Berry, N.; Limpinsel, M.; Farhi, N.; Law, M. unpublished results.
(83) Hu, J.; Zhang, Y.; Law, M.; Wu, R. *Phys. Rev. B* **2012**, *85*, 085203.
(84) Lou, L. F.; Frye, W. H. *J. Appl. Phys.* **1984**, *56*, 2253.
(85) Jones, R. E.; Yu, K. M.; Li, S. X.; Walukiewicz, W.; Ager, J. W.; Haller, E. E.; Liu, H.; Scaff, W. J. *Phys. Rev. Lett.* **2006**, *96*, 125505.
(86) Van de Walle, C. G.; Lyons, J. L.; Janotti, A. *Phys. Status Solidi A* **2010**, *207*, 1024.